Resolving buried coordination heterogeneity in $Al/AlO_x/Al$ Josephson junctions

Paul Corbae,[1,*,†] Alex Abelson,[2,†] Shivani Srivastava,[2] Heemin Lee,[1] Bevin Huang,[2] Lyrik R-J Lee,[2] Davis B. Rash,[2] Cheng-Tai Kuo,[1] Donghui Lu,[1] Mihir Pendharkar,[3,4] Loren D. Alegria,[2] Tian T. Li,[2] Keith G. Ray,[2] Shannon P. Harvey,[3] Apurva Mehta,[5] David I. Schuster,[3,4,6] Vincenzo Lordi,[2] Paul B. Welander,[3] and Jun-Sik Lee[1,‡]

[1]*Stanford Synchrotron Radiation Lightsource, SLAC National Accelerator Laboratory, 2575 Sand Hill Road, Menlo Park, California 94025, USA*
[2]*Lawrence Livermore National Laboratory, 7000 East Avenue, Livermore, California 94550, USA*
[3]*SLAC National Accelerator Laboratory, 2575 Sand Hill Road, Menlo Park, California 94025, USA*
[4]*E.L. Ginzton Laboratory, Stanford University, Stanford, California 94305, USA*
[5]*Linac Coherent Light Source, SLAC National Accelerator Laboratory, 2575 Sand Hill Road, Menlo Park, California 94025, USA*
[6]*Department of Applied Physics, Stanford University, Stanford, California 94305, USA*

(Received 5 March 2026; revised 10 June 2026; accepted 18 September 2026; published 23 October 2026)

Decoherence remains a critical obstacle to achieving high-fidelity, scalable superconducting qubits, with the tunnel barrier of Josephson junctions a key source of loss, yet the microscopic structure of this buried layer has remained difficult to probe experimentally. Here, we use resonant x-ray reflectivity to resolve the coordination environments within the AlO_x barrier of $Al/AlO_x/Al$ Josephson junctions as a function of oxidation conditions. We find that the barrier coordination evolves from more tetrahedral toward octahedral character with increasing oxidation pressure, while the lower metal-oxide interface is comparatively undercoordinated and disordered relative to the upper interface. Comparison with simulated x-ray absorption spectra identifies the dominant coordination motifs within the oxide and at its interfaces, providing depth-resolved structural insight that informs microscopic models of two-level system formation. These results link growth conditions, local coordination environments, and junction electronic properties, providing a materials-level foundation for interpreting how the tunnel barrier influences coherence in superconducting qubits.

DOI: 10.1103/lvjh-dxr8

I. INTRODUCTION

A central theme in quantum information science is the development of qubits with long coherence times and efficient control and readout [1]. Superconducting qubits incorporating $Al/AlO_x/Al$ Josephson junctions have emerged as leading candidates for scalable quantum technologies [2–4], achieving coherence times over 1 ms in several laboratories [5,6]. However, qubit coherence times and uniformity must improve to realize utility-scale quantum computation, with the junction becoming a performance-limiting factor [5]. Despite the importance of $Al/AlO_x/Al$ junctions in many modern superconducting devices, relatively little is known about their atomic scale structure. This gap in understanding motivates quantitative structural and compositional probes that can be applied directly to realistic device stacks. Here, we use resonant x-ray reflectivity to study the structure of buried $Al/AlO_x/Al$ junctions and the effect of processing variations on the dominant coordination environments of Al and O within the junction.

In superconducting qubits, parasitic two-level systems (TLS) are the dominant source of decoherence [7,8]. TLS in amorphous materials are hypothesized to be atomic-scale defects in which clusters of atoms tunnel between nearly equivalent configurations in disordered environments [9]. The amorphous oxide barrier and its interfaces with the crystalline metal electrodes host a range of atomic coordination environments that may give rise to such configurations, particularly at the metal-oxide interfaces where intrinsically perturbed coordination is expected to support a diverse landscape of local bonding configurations. Characterizing these local structural motifs is therefore a necessary step toward shedding light on the microscopic picture of junction-hosted TLS.

*Contact author: pjcorbae@slac.stanford.edu
†These authors contributed equally to this work.
‡Contact author: jslee@slac.stanford.edu

Published by the American Physical Society under the terms of the Creative Commons Attribution 4.0 International license. Further distribution of this work must maintain attribution to the author(s) and the published article's title, journal citation, and DOI.

Despite the central role of materials and interfaces in limiting qubit coherence, direct structural insight into $Al/AlO_x/Al$ junctions remains limited and is largely derived from transmission electron microscopy (TEM) and related spectroscopies [10–13]. TEM provides high spatial resolution and has yielded valuable structural insights, but sample preparation is time-intensive, and the ion milling process can introduce structural modifications or alter the composition of the Al electrodes [14]. Additionally, because TEM probes a small volume of material, individual measurements may not capture the statistical variation across an entire wafer or fully represent a particular junction growth process. Surface-sensitive techniques such as x-ray photoelectron spectroscopy have been employed successfully to help identify and eliminate lossy native oxides on superconductors within quantum circuits [15–17]. However, the short inelastic mean free path of electrons limits sensitivity to the surface [18].

Resonant x-ray reflectivity (RXR) offers a powerful approach for characterizing buried layers and interfaces by combining the depth sensitivity of nonresonant x-ray reflectivity (XRR) with the elemental and chemical sensitivity of x-ray absorption spectroscopy (XAS) [19]. By tuning the incident photon energy across the Al and O absorption edges while measuring the specular reflectivity, RXR provides depth-resolved sensitivity to variations in scattering factors associated with distinct chemical environments.

Such depth resolution is particularly critical for $Al/AlO_x/Al$ junctions, as Al oxidation follows a Cabrera-Mott mechanism in which Al ions migrate toward the oxygen-rich surface under a chemically driven potential gradient [20]. Because oxidation ceases at a thickness determined by temperature and oxygen partial pressure, this process naturally generates a compositional and coordination gradient across the oxide, with undercoordinated Al near the internal metal-oxide interface and more fully coordinated sites toward the surface [21–24]. RXR therefore provides a direct means to resolve how processing parameters influence this buried coordination landscape.

In this work, we use nondestructive, element-sensitive RXR to probe the coordination of buried $Al/AlO_x/Al$ junctions prepared under distinct oxidation conditions. Through Kramers-Kronig (KK)-constrained fitting of Al *K*-edge data, we extract layer-resolved atomic scattering factors and, by comparison with *Ab Initio* x-ray absorption spectra, identify the dominant coordination motifs in the barrier and at each metal-oxide interface. We observe a clear asymmetry between interfaces: the lower metal-oxide interface is more disordered and Al is undercoordinated, whereas the upper interface exhibits a more well-defined, higher-coordination environment. Across a series of junctions grown with increasing oxidation pressure (see Table I), the barrier coordination evolves from a mixed tetrahedral or octahedral character toward predominantly octahedral coordination. Complementary EELS measurements support these structural and chemical trends, and dc transport measurements provide an electronic perspective, from which nominal junction thicknesses and barrier heights are extracted using tunneling models. For thinner oxides, all three approaches show good agreement, whereas for thicker oxides the effective electronic thickness is smaller than that inferred from reflectivity and EELS. These results demonstrate that a layer-resolved approach of local bonding and coordination environments within the buried tunnel barrier of Josephson junctions provides inputs on models of two-level system formation, insight into processes governing barrier uniformity, and a foundation for process condition-structure correlations relevant to decoherence in superconducting qubits.

TABLE I. Junction growth conditions.

Sample ID	Oxidation condition	Junction thickness (d) (nm)
A	15 min at 4.5 Torr O_2	0.8
B	15 min at 45 Torr O_2	1.7
C	15 min at 45 Torr O_2, then 3 rounds of 1 nm Al at 0.1 nm s^{-1}, 15 min at 45 Torr O_2	4.8

II. METHODS

We fabricated a series of $Al/AlO_x/Al$ junctions on *c*-plane sapphire using double-angle electron beam evaporation described in Appendix A. X-ray studies used blanket films while dc transport measurements used small-area junctions [see Figs. 1(a)–1(c)] patterned with electron beam lithography. The $Al/AlO_x/Al$ junctions consist of a 30 nm Al layer, an oxide layer produced according to various conditions at room temperature, and a 50 nm Al cap [see Fig. 1(b)]. Additional fabrication details are provided in Appendix A.

Structural and spectroscopic characterization was carried out using RXR at Beamline 13-3 of the Stanford Synchrotron Radiation Lightsource (SSRL) at SLAC. Figure 1(c) shows the experimental geometry, in which the reflected intensity is measured under the specular condition as a function of the out-of-plane momentum transfer ($q_z = 4\pi \sin\theta/\lambda$ where λ is the wavelength and θ is the incidence angle). XRR encompasses both resonant and nonresonant measurements, whereas RXR refers specifically to measurements performed at photon energies near an absorption edge. To enhance contrast between the Al electrodes and the AlO_x junction, we used σ-polarized photons with energies spanning 1540 to 1590 eV, corresponding to the Al *K*-edge. The observed Kiessig fringes arise from interference between waves reflected at interfaces separating layers with different refractive indices.

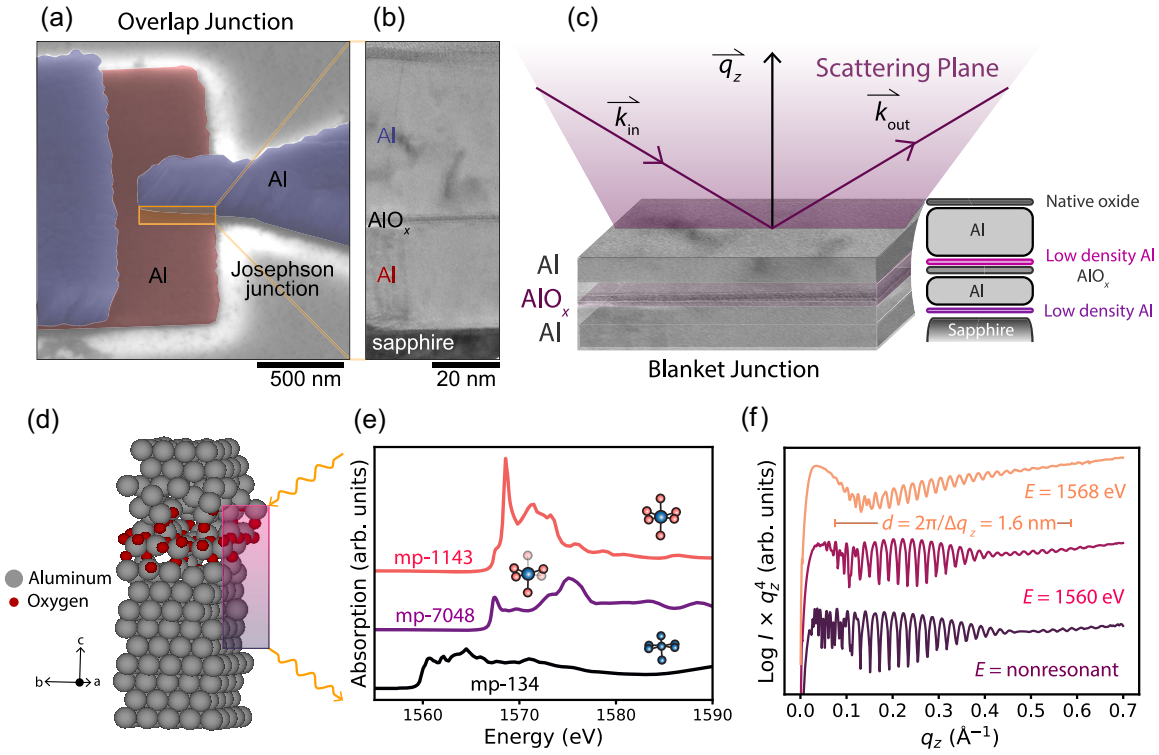


FIG. 1. Probing buried oxides in $Al/AlO_x/Al$ Josephson junctions with resonant x-ray reflectivity. (a) False-colored SEM image of a typical Josephson junction with the top electrode in purple and base electrode in red. (b) Cross-sectional TEM image of an $Al/AlO_x/Al$ junction which clearly resolves the ultrathin AlO_x tunnel barrier between the Al electrodes. (c) Schematic of the RXR geometry, where the specular reflectivity is measured under the condition $\theta_{in} = \theta_{out}$. The layer schematic shown in the figure was used for fitting XRR data. See main text for details. (d) Simulated $Al/AlO_x/Al$ junction highlighting the amorphous nature of the junction and disorder at the interfaces. (e) Calculated Al K-edge x-ray absorption near-edge spectra from the Materials Project [25–27] for metallic Al (mp-134, fcc), monoclinic Al_2O_3 (mp-7048, C2/m) with mixed tetrahedral and octahedral Al coordination, and $\alpha - Al_2O_3$ (mp-1143, corundum, R-3c) with purely octahedral Al coordination. The metallic Al spectrum exhibits a broad, featureless near-edge profile, while both oxide phases show sharper absorption features reflecting the localized Al—O bonding environments, with the monoclinic phase displaying additional spectral complexity due to its inequivalent Al sites. (f) q_z line cuts at fixed photon energies demonstrate that the Kiessig fringe periodicity evolves across the Al K-edge, with longer-wavelength oscillations at 1568 eV [red, purple in (e)] relative to 1560 eV [black in (e)], consistent with resonant modulation of the anomalous scattering factors. Rough estimation of the envelope width in q gives a junction thickness d of 1.6 nm.

For x-rays, the refractive index depends on the complex atomic scattering factors f_1 and f_2,

$$n(\omega) = 1 - \frac{n_a r_e \lambda^2}{2\pi}[f_1(\omega) - i f_2(\omega)], \tag{1}$$

where n_a is the number density and r_e is the classical electron radius. Far from absorption edges, $f_{1,2}$ exhibit only weak energy dependence; however, near a resonance, they vary strongly due to changes in the local electronic environment. The imaginary part of the atomic scattering factor, f_2, is directly related to the x-ray absorption spectrum. The XAS spectra, acquired in total electron yield (TEY) mode, were converted to f_2 and KK transformed to obtain f_1 for resonant reflectivity modeling [28].

At photon energies well away from the absorption edges, tabulated values of $f_{1,2}$ were used [29]. The underlying layer structure was first determined by fitting reflectivity scans collected at nonresonant photon energies of 1548 and 524 eV for each growth condition [30] (see Figs. 4(a), 8 for fits). The resulting structural model, illustrated in the inset of Fig. 1(c), includes the substrate, bottom electrode, junction oxide, top electrode, native oxide, and two thin interfacial layers introduced to account for reduced electron density (see Tables IV, V in Appendix H for fit parameters). The layer at the substrate-Al interface was introduced to improve fit quality, consistent with prior reports [31], while the layer above the junction derives from first-principles calculations, which predict thin regions of reduced Al density arising from the incommensurate lattice constants of Al and AlO_x, shown in Fig. 6 in Appendix E. This nonresonant refinement establishes the structural framework used in subsequent resonant (i.e., RXR) analysis.

III. RESULTS

Tuning the photon energy to an absorption edge in a reflectivity measurement (RXR) encodes the local electronic and chemical environment of each layer into the measured signal through the energy-dependent atomic scattering factors f. This is particularly relevant for amorphous AlO_x barriers [Fig. 1(d)], which host a distribution of coordination environments. As shown in Fig. 1(e), XAS spectra exhibit distinct features associated with metallic Al—Al bonding and Al-O coordination [32], providing spectroscopic fingerprints of the different local environments present within the junction. RXR therefore extends the structural information obtained from nonresonant XRR by adding sensitivity to coordination-dependent variations in bonding.

Based on these spectral features, we measure reflectivity at 1560 eV, corresponding to metallic Al-Al absorption, and at 1568 eV, associated with a sharp Al─O bonding resonance. Representative scans are shown in Fig. 1(f), with the intensity multiplied by q_z^4 to compensate for the Fresnel decay. At the AlO_x resonance (approximately 1568 eV), the reflectivity profile exhibits a low-frequency component with a characteristic length of 1.6 nm, consistent with the tunnel barrier thickness, superimposed on the high-frequency oscillations present in the nonresonant scans. In contrast, tuning to the metallic Al resonance (approximately 1560 eV) produces a profile similar to the nonresonant case. This differential response demonstrates how RXR selectively amplifies the scattering contrast of specific layers.

We extract the complex scattering factors (i.e., f_1 and f_2) of the buried oxide layer to reconstruct its layer-resolved near-edge spectral response by extending the measurement across the full Al K-edge. The resulting RXR map is shown in Fig. 2(a), where vertical cuts reproduce conventional XRR profiles as a function of q_z, while horizontal cuts trace the energy dependence of the specular reflectivity at fixed q_z. The former primarily reflects the structural layering of the junction, whereas the latter captures the resonant modulation arising from the energy-dependent dispersion (f_1) and absorption (f_2) of each layer. Two prominent features are evident in this two-dimensional RXR map. First, a clear intensity minimum appears near 1568 eV, corresponding to the strong absorption resonance at this energy, as seen in Fig. 2(b). We associate this feature with absorption by sixfold coordinated Al-O environments, consistent with the XAS spectrum in Fig. 1(e). This dip originates from strong absorption within the tunnel barrier and is distinct from the response of the metallic Al electrodes, as demonstrated by the map in Fig. 9 in Appendix I, where no dip is observed when only the metallic Al f_2 is used. Second, subtle fringe crossings emerge at low q_z near the same energy. These arise from energy-dependent phase shifts in the reflected waves due to enhanced contrast at resonance. The effect is more clearly resolved in the horizontal line cuts shown in Fig. 2(c), superimposed on the broader q_z modulation discussed above.

We determine the complex scattering factors of the buried oxide through variational fitting of the RXR maps [33–37]. This process reconstructs the near-edge spectral response of each layer within the structure, with direct sensitivity to the local coordination environment. Each layer in the reflectivity model is initialized using structural parameters obtained from the nonresonant XRR fits, including thickness, density, and roughness. The energy dependence of each layer is described by a complex atomic scattering factor, $f(\omega) = f_1(\omega) - if_2(\omega)$. For the metallic Al layers, $f(\omega)$ is taken directly from the converted XAS spectrum shown in Fig. 2(b), which is dominated by $1s \rightarrow 3p - \pi^b$ (1562.5 eV), $1s \rightarrow 3p - \sigma^*$ (1567.5 eV), and $1s \rightarrow 3d - \sigma^*$ (1573.5 eV) transitions characteristic of bulk Al; these spectral features reflect the large volume fraction of metallic Al within the limited TEY sampling depth.

For the AlO_x layer, the scattering factor is constructed as $f = 2f_{Al} + 3f_O$, with variational refinement of the spectral shape and magnitude to accommodate deviations in stoichiometry x. Deviations of each layer's $f_2(\omega)$ from the tabulated Henke values are parametrized using triangle basis functions following work by Stone *et al.* [33]. These basis functions possess analytic KK transforms, ensuring that the dispersive component $f_1(\omega)$ remains self-consistent [see Fig. 2(d)]. By fitting only the difference relative to the tabulated values, the scattering factors recover the correct asymptotic behavior far from resonance while preserving the validity of the KK relation. The resulting variational refinement reproduces the RXR map shown in Fig. 2(e).

Converged fits to the RXR maps were obtained by allowing variation in $f(\omega)$ functions of the junction oxide, native oxide, and substrate layers, as the absorption from AlO_x accounts for many of the observed features of the RXR maps (see Fig. S4 in Supplemental Material [38] and the refined native-oxide f_2). Allowing the atomic scattering factors of the low-density Al layer to vary slightly improves the goodness of fit but does not change the junction oxide's f_2, so we hold its scattering factors fixed to reduce the number of fit parameters. The resulting $f_2(\omega)$ for the buried junction layer is shown in Fig. 2(f). Comparison with both XAS spectra of bulk α-Al_2O_3 and simulation (see below) of higher-coordinated amorphous AlO_x ($CN = 5, 6$) reveals that the variationally extracted f_2 is consistent with predominantly octahedral coordination, exhibiting the characteristic sharp, two-peak structure [$1s \rightarrow 3p\sigma/\pi^*(t_{1u})$ and $1s \rightarrow 3d\sigma^*(t_{2g})$] at higher energy seen in Fig. 1(e) [32].

While the extracted $f_2(\omega)$ reflects the average coordination within the junction oxide, the layer-resolved refinement further enables us to distinguish the electronic

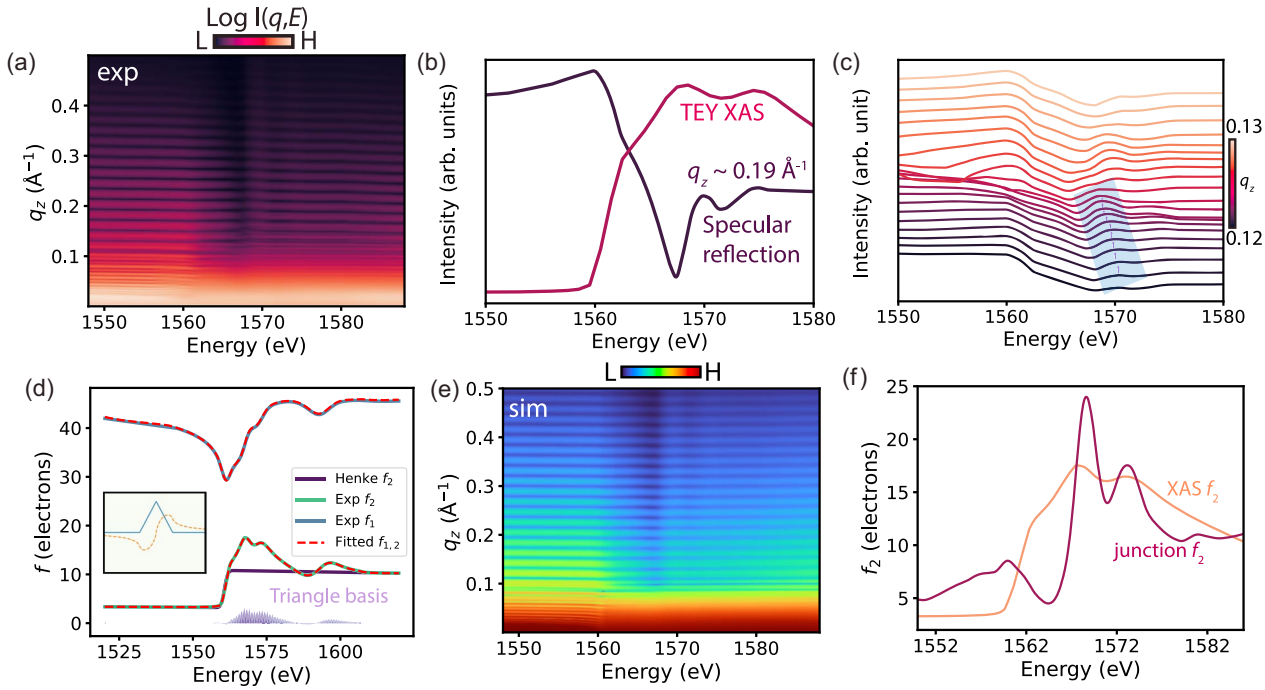


FIG. 2. Extracting the electronic structure in buried $Al/AlO_x/Al$ Josephson junctions via variational fitting of RXR maps. (a) Al K-edge RXR map for sample B, showing reflectivity attenuation near approximately 1568 and 1574 eV that fingerprints the local electronic environment. The colorbar ranges from low (L) to high (H) intensity. (b) An energy-dependent line cut at $q_z = 0.19$ Å^{-1} reveals a pronounced dip in specular reflectivity near approximately 1570 eV arising from absorption driven by the imaginary scattering factor f_2. Al K-edge TEY XAS spectrum exhibiting lineshape characteristics predominantly consistent with metallic aluminum. The dip lines up with the peak in XAS. (c) Energy-dependent line cuts at fixed q_z reveal a pronounced peak in specular reflectivity near approximately 1570 eV shifting in energy with q_z, arising from constructive interference driven by modulation of the real scattering factor f_1. (d) Atomic scattering factors $f_{1,2}$ for Al_2O_3 derived from experimental TEY XAS; triangle basis functions used to parametrize f_2 are also shown in the inset. The atomic scattering factors are expressed in units of electrons because they quantify the scattering strength of a multielectron system relative to that of a single free electron. (e) Simulated RXR map following variational refinement, capturing the reflectivity suppression at 1568 and 1574 eV. (f) Refined f_2 spectrum, compared with the f_2 derived from XAS, for the buried junction layer obtained from variational fitting, revealing distinct spectral features at energies corresponding to the observed reflectivity minima corresponding to an octahedral coordination environment.

structure of the metal-oxide interfaces from that of the interior oxide. To this end, we isolate the interfacial regions by removing 3 Å from either side of the junction oxide and treat these slices as distinct layers whose complex scattering factors are refined independently [Fig. 3(a)]. As shown in Fig. 3(b), the imaginary component f_2 at the lower interface exhibits markedly reduced spectral structure across the Al K-edge, indicative of a disordered and undercoordinated local environment. In contrast, the interior oxide retains well-defined spectral features characteristic of mixed fourfold to sixfold Al coordination, albeit with reduced relative intensity compared with fully octahedral Al_2O_3, consistent with a distorted or partially coordinated environment. The upper interface displays f_2 line shapes that more closely resemble those of a sixfold coordinated oxide, suggesting a comparatively well-ordered and densely coordinated interfacial layer.

These trends are consistent with first-principles simulations of oxide growth in Al-based Josephson junctions [24], which predict asymmetric oxygen distribution across the barrier. In those simulations, oxygen preferentially migrates toward the top electrode during growth, leading to a denser oxide at the upper interface and a more defective, undercoordinated environment at the lower interface.

To directly link RXR-derived junction f with structural models of $Al/AlO_x/Al$ junctions, we performed density functional theory (DFT) calculations and computed XAS spectra for different local coordination environments [Fig. 3(c)]. Previous DFT studies have shown that AlO_x exhibits a thermodynamic preference for amorphous films over the α and γ crystalline phases at thicknesses below 1 nm [23,39]. We employ thin-interface models with nonideal stoichiometry at the Al/AlO_x interface, as well as bulk models of stoichiometric Al_2O_3 obtained from the

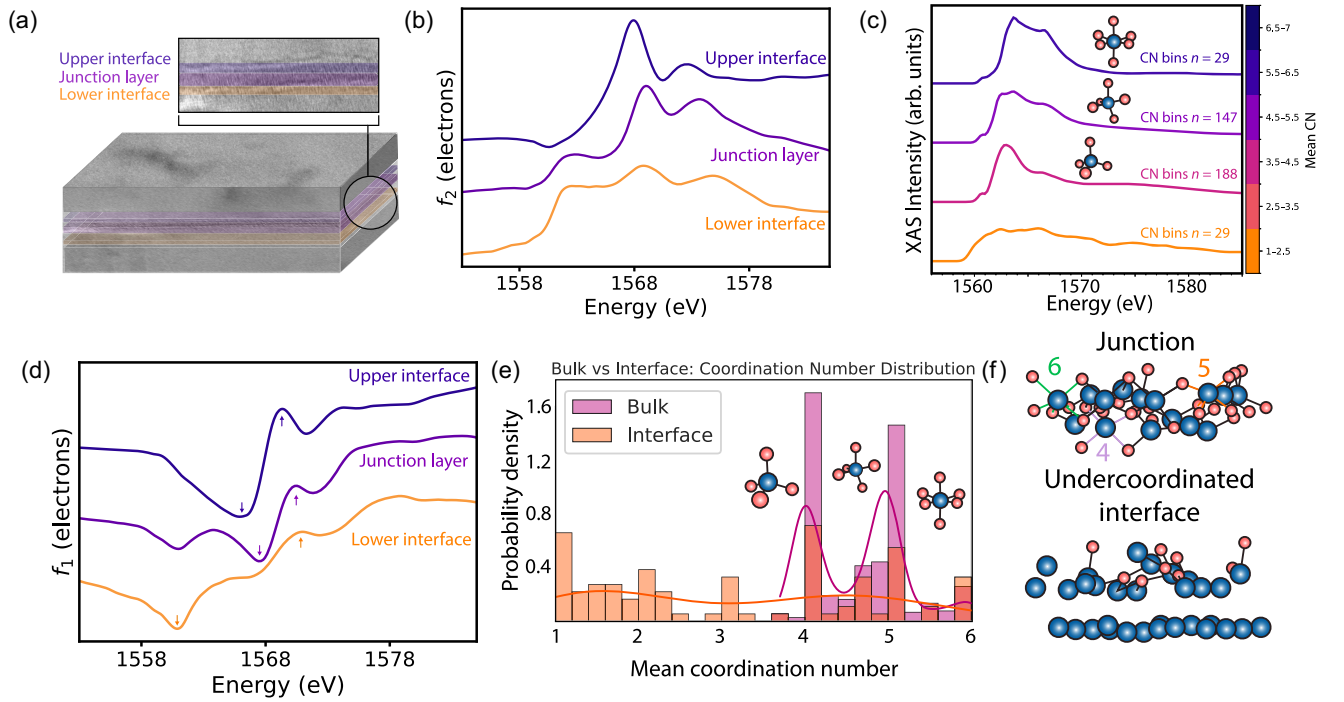


FIG. 3. Resolving the buried interface electronic structure in $Al/AlO_x/Al$ Josephson junctions. (a) Interface structure of the AlO_x barrier layer from TEM. The lower metal-oxide interface forms by oxidation of the base Al layer and is characteristically oxygen-deficient, while the upper interface is formed during Al deposition onto the completed oxide and results in structurally and chemically distinct interfaces. (b) $f_2(E)$ for the lower interface, the junction, and the upper interface. The upper interface shows a dominant sixfold coordination environment while the lower interface shows less apparent structure due to structural disorder and higher Al content. (c) Simulated XAS spectra for Al with differing coordination number. With increasing mean Al-O coordination, the spectral response evolves from a broad, weakly structured, metal-like line shape toward the pronounced two-peak oxide response characteristic of higher-coordinated Al-O. (d) $f_1(E)$ for the lower interface, the junction, and the upper interface [same color map as (b)]. The upper interface shows a high effective electron density near 1568 eV where the lower interface shows low effective electron density near 1560 eV as large variations in f_2 drive correspondingly large changes in f_1 through KK relations. Curves are offset by a constant amount for visual clarity. (e) Coordination environment analysis for bulk and interfacial AlO_x in simulated Josephson junctions. The interface exhibits a broad distribution of local coordination environments spanning onefold to sixfold, whereas the bulk is confined predominantly to fourfold to sixfold sites. The curves are the probability distribution function from the histograms. (f) First-principles derived snapshots of different regions in the AlO_x junction. Tetrahedral, trigonal bipyramidal, octahedral (4,5,6) environments are highlighted.

Materials Project database [40], to calculate theoretical x-ray absorption spectra using DFT. Continuous symmetry measure (CSM) analysis [41] is performed to treat distorted Al-O coordination environments and to smoothly interpolate between nominal integer coordination numbers (see Appendix E).

The calculated spectra reveal systematic trends with coordination number. The general trend is that the main absorption peak shifts to higher energy and the spectrum develops additional structure as the Al-O coordination increases, highlighting the sensitivity of the near-edge response to local bonding geometry. A pronounced preedge or shoulder feature appears for mean Al coordination numbers of approximately 3.5–4.5, with additional weaker contributions arising from distorted sixfold environments. These spectral variations reflect changes in Al $3s-$ O $3p$ hybridization associated with reduced symmetry, enabling transitions absent in the undistorted octahedral environments of crystalline α-Al_2O_3. For higher-coordination environments (fivefold to sixfold), a broader secondary peaklike feature emerges at higher energies. The coordination-number distribution also varies with local chemistry: interface regions contain a substantial population of undercoordinated Al sites (absent in stoichiometric amorphous Al_2O_3), giving rise to the distinct spectral fingerprints that we observe. Comparison of the extracted f_2 with the calculated XAS indicates that the lower interface is comparatively undercoordinated, whereas the bulk of the junction and the upper interface have higher-coordinated Al environments. Individual spectral features may additionally arise from symmetry-specific transitions associated with distinct local geometries, such as tetrahedral or octahedral environments.

This interpretation is further corroborated by the behavior of f_1 across the junction, shown in Fig. 3(d). In the oscillator model, $f_1(\omega)$ approaches Z in the high-frequency limit of $\omega^2 \gg \omega_s^2$, where ω_s is the resonance frequency. Near an absorption edge, the real part of the atomic scattering factor deviates sharply from Z, and the quantity $f_1(\omega) = Z + \Delta f_1(\omega)$ can be interpreted as an effective scattering charge that depends on photon energy. Within this framework, the lower interface exhibits reduced effective electron density at photon energies corresponding to metallic Al and an increase at photon energies associated with AlO_x. Taken together, the trends in the DFT and RXR-derived f_2 indicate that the bulk of the junction in this sample (sample B) is predominantly octahedrally coordinated, though with possible contributions from near-octahedral sites (fivefold). Additionally, there is a redistribution of electronic charge and local bonding character at the lower interface, consistent with an oxygen-deficient, metal-proximal environment that is electronically distinct from both the bulk junction oxide and the more fully coordinated upper interface, shown in Figs. 3(e) and 3(f), in agreement with previous computational and experimental studies [21–23]. This interfacial asymmetry underscores that the buried barrier cannot be regarded as structurally uniform, even at subnanometer thicknesses.

Having established the coordination environment of the junction oxide, we now examine how it evolves under different oxidation conditions, Table I.

Correlating the coordination environment with device performance metrics in future work would offer a route toward identifying fabrication conditions associated with reduced TLS-relevant structural disorder. Figure 4(a) shows the nonresonant XRR data for each of the samples within the growth series. Comparing the three sample types, we observe a monotonic increase in the junction thickness from 0.8 to 1.8 to 4.75 nm for A, B, and C, respectively, as the oxidation conditions become progressively more aggressive.

Figure 4(b) shows resonant XRR maps from three samples within the junction growth series (A, B, and C). There are subtle variations in the specular reflectivity across the series, reflecting distinct electronic environments in the buried junction layers of each film. Additionally, sample A shows an intensity peak around 1580 eV, indicative of redistributed spectral weight at

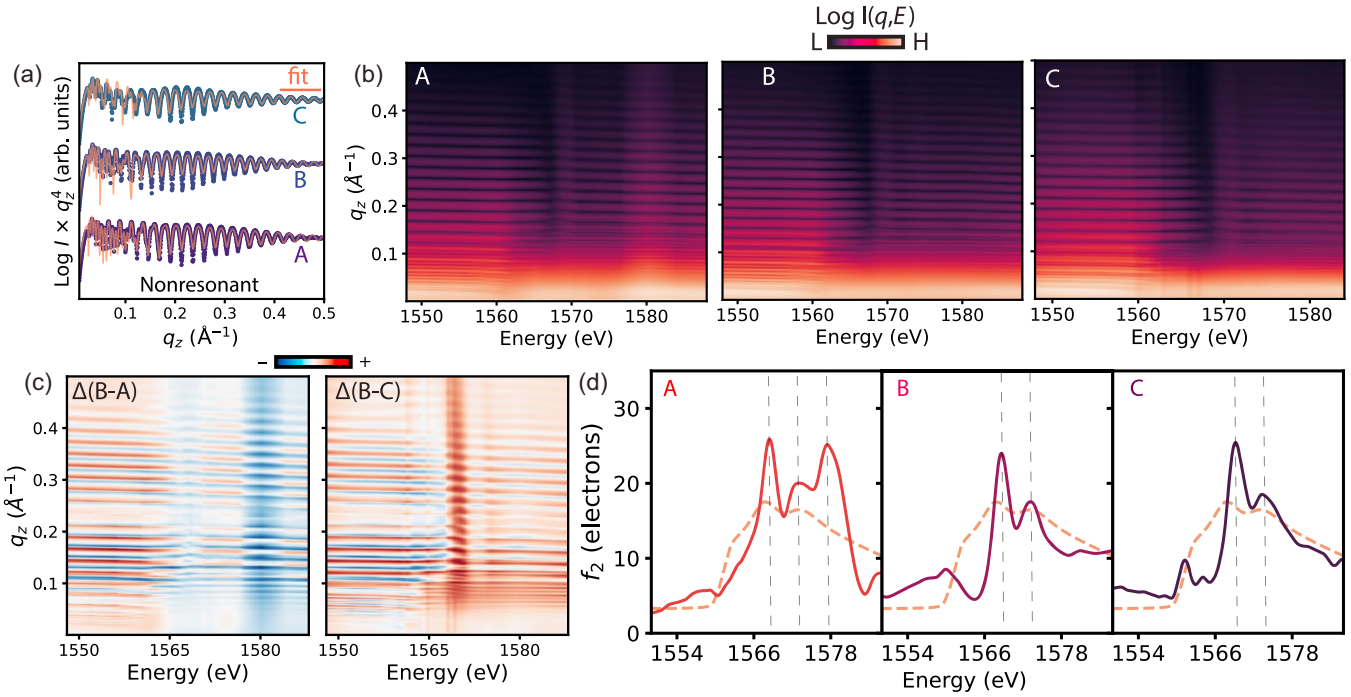


FIG. 4. Growth-dependent electronic structure of $Al/AlO_x/Al$ Josephson junctions probed by Al K-edge RXR. (a) Nonresonant XRR measured below the Al K-edge with the corresponding structural fit for samples A, B, and C. (b) Al K-edge RXR maps across the junction growth series. With increasing O_2 pressure, the reflectivity exhibits enhanced attenuation near approximately 1568 eV and a suppression of the feature around approximately 1577 eV, indicating systematic changes in the local electronic environment. (c) Difference maps between samples B-A as well and B-C highlight pronounced energy-dependent modulations, reflecting variations in the electronic structure and coordination of the buried oxide layer as well as structural parameters. (d) The extracted $f_2(E)$ of the buried junction layer for A, B, and C as well as the initial condition $f_2(E)$ extracted from the XAS. The $f_2(E)$ moves from having three main peaks in A to two main peaks in B/C representing a change in local coordination from a mixture of tetrahedral and octahedral to mostly octahedral.

higher energies. A difference map between samples A and B RXR maps [Fig. 4(c)] highlights differences both structurally in the q_z direction and electronically in the E direction. To fully register the differences between sample types, we perform variational fitting of the other two samples.

Figure 4(d) shows the complex parts of the scattering factors for the buried oxide layer of each of the three samples. The f_2 spectra exhibit clear differences across growth conditions. In particular, f_2 evolves from three distinct peaks at 1568.5, 1573.0, and 1577.7 eV in sample A to two peaks at 1568.5 and 1573 eV in samples B and C. The f_2 spectra for samples B and C closely resemble the XAS spectrum of sixfold coordinated AlO_x and are consistent with the DFT [Fig. 3(c)]. In contrast, sample A exhibits an additional higher-energy feature reminiscent of the third peak in γ-Al_2O_3 (attributed to Al 1s transitions into final states with Al 3d tetrahedral symmetry), suggesting an increased fraction of tetrahedral local coordination compared with octahedral [24,32,42]. This high-energy feature should be distinguished from the general coordination-dependent evolution of the dominant absorption response: it arises from a symmetry-specific transition associated with tetrahedral Al-O environments, whereas the two dominant features near 1568.5 and 1573 eV are characteristic of predominantly octahedral Al-O environments. These systematic spectral changes reveal that increasing oxidation pressure shifts the coordination landscape of the barrier from a mixed tetrahedral or octahedral environment toward predominantly octahedral coordination.

As an independent probe of local structure, we used electron energy loss spectroscopy (EELS) to examine the electron energy loss near-edge structure (ELNES) of the Al $L_{2,3}$ and O K edges [Fig. 5(a)]. Al L-edge ELNES has been used to qualitatively assess the coordination environment and chemical homogeneity of AlO_x JJs [43–45]. Aluminum oxide polymorphs exhibit distinct near-edge spectral signatures associated with the local coordination of Al [46,47]. In bulk crystals, tetrahedral coordination typically produces a weak peak or shoulder near 78 eV and a stronger peak near 80 eV, whereas octahedral coordination (e.g., α-Al_2O_3) produces a strong peak near 79 eV with a shoulder near 80 eV [46]. In JJs, both the relative intensities and energies of these near-edge features have been used as qualitative indicators of local coordination.

Our ELNES data are qualitatively consistent with previous reports, exhibiting a weak peak or shoulder at 77.7 eV and a stronger peak near 80 eV [Fig. 5(b)]. The low-energy feature is consistent with a fraction of tetrahedrally coordinated Al within the oxide, although its abundance cannot be determined directly from these spectra. Quantitative interpretation likely requires simulations that account for the structure of the buried oxide, including short- and medium-range order [48], dangling bonds, and other structural inhomogeneities. The O K-edge ELNES provides less direct discrimination between coordination environments [12,44,49,50]. Thus, while ELNES provides qualitative sensitivity to local coordination through peak energies and relative intensities, Al K-edge x-ray spectroscopy exhibits more clearly resolved coordination-dependent spectral features, enabling a more direct identification of local bonding configurations [12,13,43,44,49,50].

Finally, to directly probe the electronic properties of each sample type, we patterned shadow-evaporated Josephson junctions [Fig. 1(a)] and performed current-voltage (I-V) measurements. Junction barrier height and thickness were extracted by fitting I-V data to the Simmons tunneling model [51], as shown in Fig. 5(c). The extracted mean thickness is 1.12 and 1.18 nm for samples A and B,

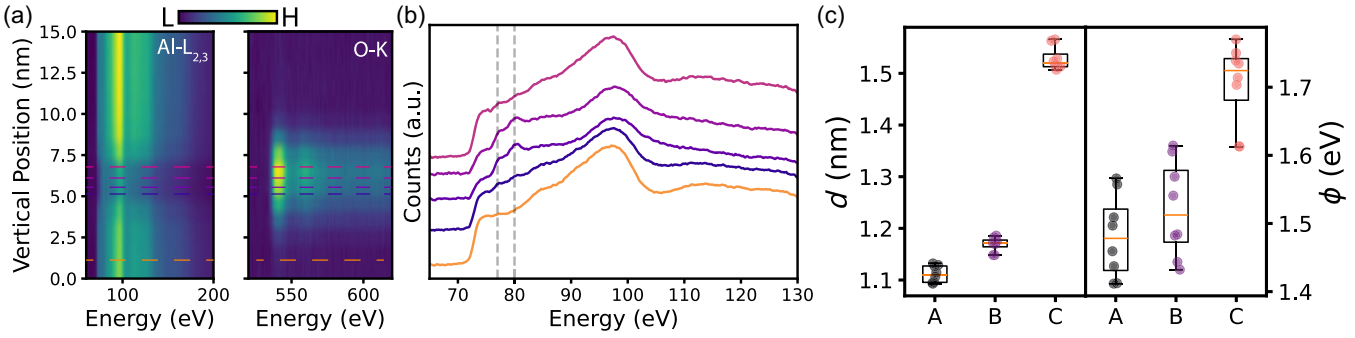


FIG. 5. Benchmarking RXR with ELNES and I-V characterization of Al/AlO_x/Al Josephson junctions. (a) Al $L_{2,3}$-edge of B showing clear intensity change across the junction oxide, with either side displaying metallic aluminum line shapes. O K-edge of sample B showing clear O intensity in the junction, exactly where the Al $L_{2,3}$-edge shows a decrease in intensity. (b) Specific Al $L_{2,3}$-edge line cuts in the junction and the Al metal. The JJ oxide has peaks at approximately 77 and 80 eV whose ratio determines the ratio of tetrahedral to octahedral environments. Line color corresponds to the dashed line in (a). (c) Simmons model fits to the measured current-voltage characteristics for the junction series. Both the extracted barrier thickness, d, and barrier height, ϕ, increase with increasing oxidation pressure, consistent with the growth of a thicker, more fully oxidized tunnel barrier.

respectively, and increases to 1.52 nm for sample C. The significant disparity in RXR and Simmons model-derived thickness for sample C is likely due to the combination of increased junction roughness and the exponential dependence of tunneling current on thickness: thinner regions disproportionately dominate the electrical response. The extracted barrier heights in samples A, B, and C increase from 1.48 to 1.52 and 1.73 eV. This trend is consistent with improved oxidation and a reduction in defect-assisted tunneling and a more insulating, bulklike oxide.

IV. DISCUSSION

The evolution from a three- to two-peak profile in f_2 across samples A–C indicates that the amorphous AlO_x barrier becomes increasingly octahedrally coordinated with oxidation pressure, while sample A retains a larger fraction of tetrahedrally coordinated Al sites. This trend is consistent with our finding that the lower metal-oxide interface is undercoordinated: for the thinnest barrier and lowest oxidation pressure (sample A), a greater proportion of the oxide volume lies in proximity to this interface, shifting the coordination toward lower values. It is particularly noteworthy that samples B and C exhibit similar scattering factors given their distinct growth conditions, although they share a high oxygen pressure (45 Torr), suggesting that coordination environment may be more sensitive to oxygen partial pressure during oxidation than total film thickness. The O K-edge variational fits further corroborate this picture, showing that the dominant peak in f_2 is shifted toward lower photon energies for samples B and C, consistent with a more sixfold-coordinated local environment [32] (see Fig. S2 in Supplemental Material [38]). Differences in interface structures and variation of interface participation in junction properties may vary with thickness, for typical oxidation conditions.

There are apparent prepeak features in the extracted f_2 of the buried junction layers at 1562 and 1564 eV. The prepeak at 1562 eV can be attributed to a trigonal bipyramid coordination (fivefold) environment, which can be expected in an amorphous layer [52]. The prepeak observed at 1564 eV [$1s \rightarrow 2s\sigma^*(a_{1g})$] has been ascribed to thermally induced lattice vibrations that amplify octahedral distortions, thereby facilitating enhanced sp hybridization at the lower edge of the conduction band [53–55]. The extent to which the variational fitting technique is sufficiently sensitive to resolve such subtle prepeak modifications in the electronic structure remains uncertain and should be rigorously validated through its application to a broader range of systems, though this prepeak feature is captured in our first-principles result, Fig. 3(c).

Previous studies of the near-edge features of the EELS spectra combined with a pair distribution function analysis from nanobeam diffraction data indicate tetrahedrally coordinated Al atoms in the barrier interior, consistent with amorphous aluminum oxide, but less coordination near the interface, indicative of oxygen vacancies [11]. It has been shown with ELNES that atomic-layer deposited (ALD) Al_2O_3 contains both tetrahedral and octahedral coordination environments, with octahedral Al dominating away from the interface (deeper in the junction), while the interfacial region is comparatively undercoordinated and richer in tetrahedral Al [43]. These results for ALD Al_2O_3 are consistent with our findings that in the thicker junctions grown with higher O_2 pressure the environment is more octahedral, whereas in the thinner junctions it looks more tetrahedral, Figs. 1(d) and 4(d). It has been demonstrated that replacing amorphous AlO_x with a single-crystal epitaxial Al_2O_3 tunnel barrier, with an octahedral environment, in Josephson junction qubits reduces the density of decoherence-inducing two-level fluctuators by approximately 80% [56]. The results presented here indicate that oxidation conditions systematically influence the local coordination landscape of the barrier, and with it the types of defect configurations implicated in TLS formation. Establishing a direct link to qubit coherence, however, will require further device-level investigation.

V. CONCLUSION

This work represents a direct application of x-ray scattering and spectroscopy to nondestructively resolve the coordination environment and microscopic structure of the buried oxide barrier in Al-based Josephson junctions. Using Kramers-Kronig-constrained variational fitting of resonant x-ray reflectivity maps across the Al K-edge, we extracted the layer-resolved atomic scattering factors of the buried AlO_x barrier and, through comparison with *ab initio* x-ray absorption spectra, identified the dominant coordination motifs in the bulk oxide and at each metal-oxide interface. Across a series of junctions grown under varying oxidation conditions, we find that the barrier coordination evolves from more tetrahedral toward predominantly octahedral character with increasing oxidation pressure, while the lower metal-oxide interface remains consistently more disordered and undercoordinated than the upper interface. EELS and I-V measurements independently confirm these structural trends and connect the structure variations to differences in junction electrical characteristics (barrier height). Through systematic variation of growth parameters, we demonstrate how oxidation conditions dictate the local coordination environment of the buried tunnel barrier, providing the structural inputs that microscopic models of TLS formation can be tested against. The undercoordinated lower interface dominates the coordination landscape of thin tunnel barriers, identifying more aggressive oxidation as a route to a more structurally homogeneous, octahedrally coordinated AlO_x barrier. Looking forward, RXR opens opportunities to explore more ambitious process variations: alternative barrier materials, oxidation schemes, and epitaxial

interfaces with the spectroscopic precision necessary to guide rational optimization, with relatively high throughput and large sampling area. Thus, RXR provides a nondestructive, depth-resolved structural characterization tool for Josephson junction tunnel barriers and a foundation for future work linking barrier structure to device-level coherence measurements.

ACKNOWLEDGMENTS

We thank Kevin Stone for helpful discussion regarding variational fitting and Cheng Peng for help running FEFF calculation. The RXR experiments were carried out at the SSRL (beamline 13-3), SLAC National Accelerator Laboratory, supported by the U.S. DOE, Office of Science, Office of Basic Energy Sciences under Contract No. DE-AC02-76SF00515. This work was also supported by the auspices of the U.S. Department of Energy by Lawrence Livermore National Laboratory under Contract No. DE-AC52-07NA27344. The measured junctions are based upon work supported by the Air Force Office of Scientific Research under Award No. FA9550-23-1-0692.

P. C., A. A., S. S., A. M., P. W., V. L., and J. S. L. conceived the project. P. C., H. L., C. T. K., and J. S. L. performed the XRR measurements. A. A., D. R., B. H., and L. R. L. performed the growth, fabrication, and transport. S. S. performed the DFT calculations. All authors contributed in discussing the results and forming conclusions.

DATA AVAILABILITY

The data that support the findings of this article are not publicly available. The data are available from the authors upon reasonable request.

APPENDIX A: RXR SAMPLE FABRICATION

All RXR samples were fabricated on *c*-plane sapphire wafers (HEMEX, Crystal Systems) annealed at 1000 °C in flowing O_2 for 2 h. A 230-nm Ta film (99.95% purity) was sputtered in a Kurt Lesker PRO Line PVD 75 at a sample temperature of 625 °C. The wafer was patterned using AZ1518 positive photoresist with a Heidelberg MLA maskless aligner. The resist image was puddle developed with MIF 917, then rinsed with DI water. The Ta was dry-etched with SF_6 in an Ulvac NE-550EXa inductively coupled plasma etcher. Following the etch, residual resist was removed through sonication in acetone, followed by a rinse in DI water. The wafer was then soaked in hot piranha ($3\,H_2SO_4 : 1\,H_2O_2$) for 15 min, followed by a 5 min immersion in 6:1 buffered oxide etchant. The wafer was thoroughly rinsed with DI water, dried under flowing N_2, then placed on a 110 °C hotplate for 1 min. Less than 3 min elapsed between drying and spinning of resist.

TABLE II. Junction growth conditions.

Sample ID	Oxidation condition
X	15 min at 0.45 Torr O_2
A	15 min at 4.5 Torr O_2
B	15 min at 45 Torr O_2
C	15 min at 45 Torr O_2, then 3 rounds of 1 nm Al at 0.1 nm s^{-1}, 15 min at 45 Torr O_2

LOR10B (Microchem) was spin coated at 3000 rpm, then soft-baked for 5 min at 170 °C. Next, S1805 (Microposit) was spin coated at 2000 rpm and baked for 1 min on a hot plate at 115 °C. The resist was exposed with a Heidelberg MLA maskless aligner, developed in an 8.5:1.5 solution of CD-26:DI water, then rinsed with DI water. The wafer was then loaded into a PLASSYS MEB550 electron beam deposition tool and mounted with a custom four-way physical mask that exposes only 1/4 of the wafer during a deposition. Each of the four depositions was identical, except for the oxidation step, as noted in Table I. The load lock was pumped to 7×10^{-7} Torr, then exposed to a 5 min UV ozone treatment at 7.5 Torr O_2. A 4 min Ti gettering step was performed immediately prior to Al deposition. The wafer was tilted to 25° and 30 nm of Al was deposited. Next, the wafer was oxidized under the conditions described in Table I. After oxidation, the wafer was tilted to −25° and 50 nm of Al was deposited. Finally, the film was oxidized for 15 min at 75 Torr. See Table II.

After deposition the wafer was diced, then lifted off with heated Remover PG (Kayaku), followed by an additional brief soak in neat Remover PG, then two sequential isopropanol baths. The chips were individually dried under flowing N_2, then stored in an Ar environment prior to x-ray measurements.

APPENDIX B: DC TRANSPORT SAMPLE FABRICATION

AlO_x junctions were deposited onto *c*-plane sapphire substrates prepatterned with Ta contact pads. MMA(8.5) MAA EL13 (Microchem) was spin coated onto the wafer and baked at 180 °C. The same process was repeated for AR-P 672.045 (AllResist GmbH). A conductive Al layer was electron beam evaporated onto the wafer. Next, the wafer was patterned by electron beam lithography (Raith EBPG) and developed in a mixture of water and isopropanol. Junction deposition proceeded identically to the RXR samples, as did dicing and liftoff.

APPENDIX C: X-RAY MEASUREMENTS

The junctions were held at a temperature of 13 K in UHV and investigated using a beam spot of approximately $300 \times 300\ \mu m^2$. Measured XRR blanket films were

8×12 mm. The scattered photons were detected using a GaAsP photodiode. Multilayer reflectivity was calculated using the Parratt recursion formalism [57], where the optical constants of each layer, $f_{1,2}(\omega)$, are allowed to vary in the fit.

APPENDIX D: TEM AND ELECTRON ENERGY LOSS SPECTROSCOPY

TEM measurements were obtained using a Thermo Fisher Titan 80–300 (scanning) transmission electron microscope, operated at 300 kV. EELS data were collected in STEM mode, with a Gatan GIF Quantum ER spectrometer. EELS zero-loss peak (ZLP) has a full width at half maximum of 0.9 eV and the GIF was operated in dual EELS mode to capture both ZLPs and corresponding core-loss spectra. EELS ELNES were extracted by performing Fourier-Ratio method to remove sample thickness effect.

APPENDIX E: DENSITY FUNCTIONAL THEORY AND SIMULATION

Amorphous oxide structures were obtained from the Materials Project database [40], and interface models were generated from our DFT molecular dynamics simulations of oxide growth using methods described in our previous work [22]. All DFT calculations employed the PAW method and GGA exchange correlation approximation as implemented within VASP [58–63]. Thermal broadening was accounted for in each model for bulk and interface using NVT molecular dynamics for 10 ps with a 2 fs time step, from which 20 snapshots were uniformly sampled. For interface structures, structural relaxation and MD sampling were performed using our in-house trained MACE interatomic potential [64,65] (details will be subject of future work). Brillouin-zone sampling used $3 \times 3 \times 3$ k-point meshes for amorphous bulk and $2 \times 2 \times 1$ for interface models, and PAW pseudopotentials `Al_GW` and `O_GW` were employed throughout.

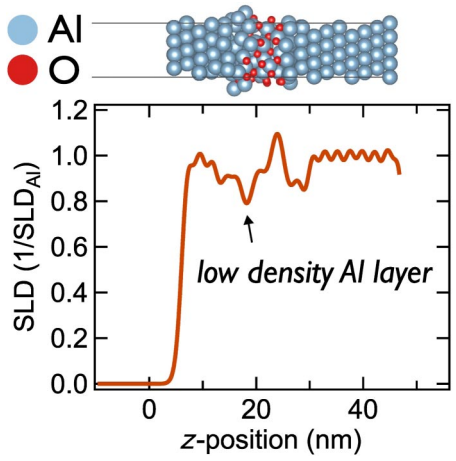


FIG. 6. Junction SLD.

XANES spectra were computed within VASP using the final-state core-hole approximation [66,67], in which a core electron is promoted into the conduction manifold and a full K-edge core hole is applied to the absorbing atom. The calculation included explicit evaluation of transition matrix elements between the core and unoccupied states, and intrinsic spectral broadening was controlled using VASP's internal Gaussian broadening scheme. The unoccupied density of states was sampled with high resolution to obtain smooth spectra, and standard electronic self-consistency parameters appropriate for PAW-based x-ray spectroscopy were employed. For each absorbing site, spectra were averaged over 20 MD snapshots, and all results were rigidly aligned such that the first absorption peak coincided with the corresponding VASP reference.

CSM analysis [41] was used to assign Al and O coordination numbers by comparing each local Al-O environment to ideal reference polyhedra using a Voronoi-based neighbor definition. A maximum distance factor of 1.4 and a 4.0 Å Voronoi cutoff were used with the element pair restricted to Al and O.

APPENDIX F: ELECTRICAL CHARACTERIZATION

The current-voltage (I-V) characteristics of Josephson junctions were measured at room temperature using a Keithley 2612B source measure unit. The voltage was swept from -1 to 1 V in 10 mV steps at a sweep rate of 0.6 V/s. The I-V traces were fit with a symmetric barrier Simmons tunneling model according to the following expression:

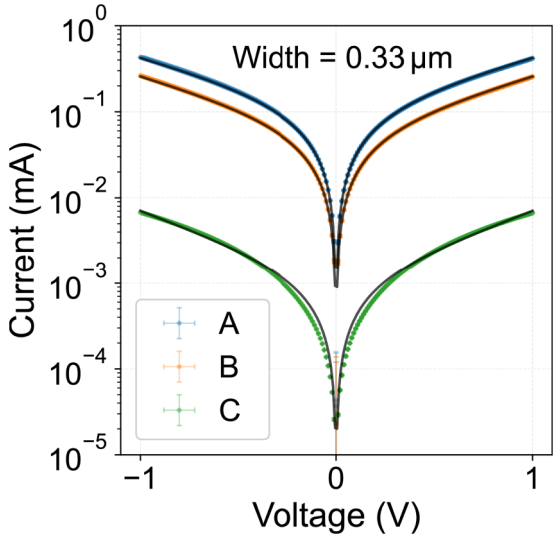


FIG. 7. Simmons model. Thickness and barrier height extracted from fitting I-V curves with the Simmons model. Using a $m^* = 0.4m_e$.

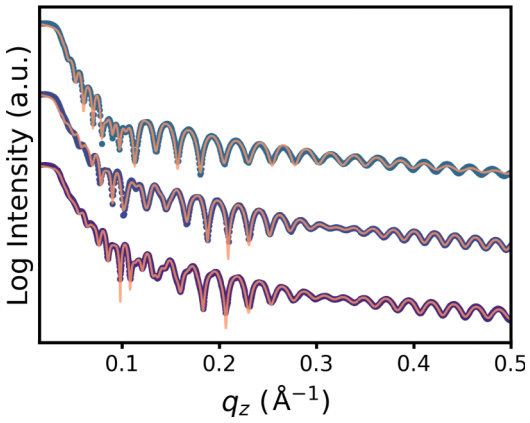


FIG. 8. Oxygen nonresonant XRR fit. Top to bottom: C, B, A. The orange lines are fits. $h\nu = 500$ eV.

$$I = \frac{eA}{2\pi h d^2}\left(\left(\phi - \frac{eV}{2}\right)\exp\left[-\frac{4\pi d}{h}\sqrt{2m^*\left(\phi - \frac{eV}{2}\right)}\right] - \left(\phi + \frac{eV}{2}\right)\exp\left[-\frac{4\pi d}{h}\sqrt{2m^*\left(\phi + \frac{eV}{2}\right)}\right]\right), \tag{F1}$$

where I is the measured current, A is the nominal area, h is Planck's constant, d is the barrier thickness, $m* = 0.4$ is the approximated effective mass of the junction oxide, and ϕ is the barrier height. Only ϕ and d are allowed to vary during fitting, with the area A determined experimentally from SEM images. See Fig. 7 for fits.

APPENDIX G: THICKNESS FROM DIFFERENT MEASUREMENTS

To directly probe the electronic properties of each sample type, we prepared shadow-evaporated Josephson junctions following identical oxide growth procedures and probed their room temperature resistance. We fit current-voltage curves with the Simmons tunneling model [51], from which we can extract barrier heights ϕ and junction thicknesses d. The extracted thickness increases from 1.12 to 1.52 nm, remaining systematically smaller than the values obtained from XRR and TEM, particularly for sample C. This discrepancy likely arises from the deposition geometry: the angles involved during sequential Al deposition and subsequent oxidation result in an effectively reduced oxide thickness. The barrier height increases from 1.48 to 1.73 eV with increased thickness, which is consistent with enhanced oxidation and improved stoichiometry of the AlO_x barrier, leading to a reduction in defect-assisted tunneling and a more insulating, bulklike oxide. See Table III.

TABLE III. Junction thickness measurements.

	Transport (nm)	X-ray (nm)	TEM (nm)
A	1.12	0.8	NA
B	1.18	1.7	∼2
C	1.52	4.8	∼5

APPENDIX H: XRR FITTING PARAMETERS

TABLE IV. Al *K*-edge sample parameters.

Parameter	A	B	C
Native oxide n (atoms/Å^3)	0.01513	0.01404	0.01416
Native oxide d (Å)	23.59	18.4	32.69
Native oxide σ (Å)	12.73	15.63	15.65
Upper Al n (atoms/Å^3)	0.05	0.06312	0.04909
Upper Al d (Å)	484.5	471	504.5
Upper Al σ (Å)	14.69	17.13	16.32
Junction n (atoms/Å^3)	0.02374	0.024	0.02053
Junction d (Å)	8.076	17.52	48.95
Junction σ (Å)	1.833	4.074	10.96
Lower Al n (atoms/Å^3)	0.05	0.07272	0.05006
Lower Al d (Å)	266.8	263	268.5
Lower Al σ (Å)	8.485	29.98	3.867
Upper low density Al n (atoms/Å^3)	0.02852	0.04378	0.04992
Upper low density d (Å)	5.001	19.53	19.08
Upper low density Al σ (Å)	12	3.436	2.526
Lower low density Al n (atoms/Å^3)	0.028	0.03487	0.01126
Lower Low density Al d (Å)	3	5.521	1.068
Lower low density Al σ (Å)	5	3.601	9.93
Substrate σ (Å)	3.846	0.7521	1.848

TABLE V. O *K*-edge sample parameters.

Parameter	A	B	C
Native oxide n (atoms/Å^3)	0.01194	0.01404	0.02349
Native oxide d (Å)	18.76	18.4	39.98
Native oxide σ (Å)	11.93	15.63	22.86
Upper Al n (atoms/Å^3)	0.07489	0.06312	0.08
Upper Al d (Å)	482	471	471.2
Upper Al σ (Å)	17.22	17.13	19.92
Junction n (atoms/Å^3)	0.0173	0.024	0.01082
Junction d (Å)	11.94	17.52	47.49
Junction σ (Å)	12.71	4.074	9.967
Lower Al n (atoms/Å^3)	0.06643	0.07272	0.0516
Lower Al d (Å)	253.6	263	251.6
Lower Al σ (Å)	3.708	29.98	5.003
Upper low density Al n (atoms/Å^3)	0.05613	0.04378	0.06496
Upper low density d (Å)	8.22	19.53	16.95
Upper low density Al σ (Å)	3.005	3.436	9.994
Lower low density Al n (atoms/Å^3)	0.02014	0.03487	0.03777
Lower Low density Al d (Å)	3.993	5.521	8.684
Lower low density Al σ (Å)	6.203	3.601	0.5011
Substrate σ (Å)	1.132	0.7521	0.7561

APPENDIX I: RXR MAP FITTING

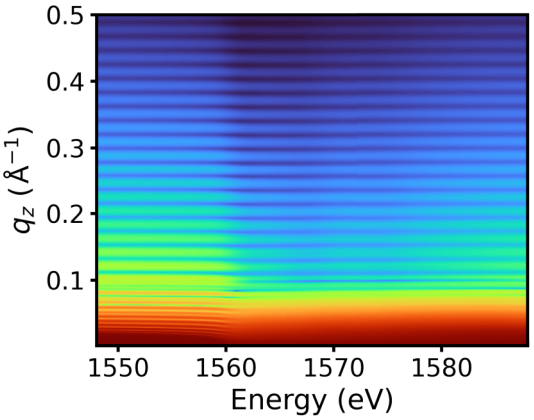


FIG. 9. RXR map before variational fitting. Sample B simulation uses the f_2 generated from the TEY XAS.

[1] M. H. Devoret and R. J. Schoelkopf, Superconducting circuits for quantum information: An outlook, Science **339**, 1169 (2013).

[2] W. D. Oliver and P. B. Welander, Materials in superconducting quantum bits, MRS Bull. **38**, 816 (2013).

[3] P. Krantz, M. Kjaergaard, F. Yan, T. P. Orlando, S. Gustavsson, and W. D. Oliver, A quantum engineer's guide to superconducting qubits, Appl. Phys. Rev. **6**, 021318 (2019).

[4] M. Kjaergaard, M. E. Schwartz, J. Braumüller, P. Krantz, J. I.-J. Wang, S. Gustavsson, and W. D. Oliver, Superconducting qubits: Current state of play, Annu. Rev. Condens. Matter. Phys. **11**, 369 (2020).

[5] M. P. Bland, F. Bahrami, J. G. Martinez, P. H. Prestegaard, B. M. Smitham, A. Joshi, E. Hedrick, S. Kumar, A. Yang, A. C. Pakpour-Tabrizi *et al.*, Millisecond lifetimes and coherence times in 2D transmon qubits, Nature (London) **647**, 343 (2025).

[6] M. Tuokkola, Y. Sunada, H. Kivijärvi, J. Albanese, L. Grönberg, J.-P. Kaikkonen, V. Vesterinen, J. Govenius, and M. Möttönen, Methods to achieve near-millisecond energy relaxation and dephasing times for a superconducting transmon qubit, Nat. Commun. **16**, 5421 (2025).

[7] C. Müller, J. H. Cole, and J. Lisenfeld, Towards understanding two-level-systems in amorphous solids: Insights from quantum circuits, Rep. Prog. Phys. **82**, 124501 (2019).

[8] J. Lisenfeld, A. K. Händel, E. Daum, B. Berlitz, A. Bilmes, and A. V. Ustinov, Mapping the positions of two-level-systems on the surface of a superconducting transmon qubit, npj Quantum Inf. **12**, 80 (2026).

[9] Z. Wang, C. C. Yu, and R. Wu, Why superconducting Ta qubits have fewer tunneling two-level systems at the vacuum-oxide interface than Nb qubits, Phys. Rev. Appl. **23**, 024017 (2025).

[10] L. J. Zeng, P. Krantz, S. Nik, P. Delsing, and E. Olsson, The atomic details of the interfacial interaction between the bottom electrode of $Al/AlO_x/Al$ Josephson junctions and HF-treated Si substrates, J. Appl. Phys. **117**, 163915 (2015).

[11] L. Zeng, D. T. Tran, C.-W. Tai, G. Svensson, and E. Olsson, Atomic structure and oxygen deficiency of the ultrathin aluminium oxide barrier in $Al/AlO_x/Al$ Josephson junctions, Sci. Rep. **6**, 29679 (2016).

[12] S. Fritz, A. Seiler, L. Radtke, R. Schneider, M. Weides, G. Weiß, and D. Gerthsen, Correlating the nanostructure of Al-oxide with deposition conditions and dielectric contributions of two-level systems in perspective of superconducting quantum circuits, Sci. Rep. **8**, 7956 (2018).

[13] D. P. Pappas, M. Field, C. J. Kopas, J. A. Howard, X. Wang, E. Lachman, J. Oh, L. Zhou, A. Gold, G. M. Stiehl, K. Yadavalli, E. A. Sete, A. Bestwick, M. J. Kramer, and J. Y. Mutus, Alternating-bias assisted annealing of amorphous oxide tunnel junctions, Commun. Mater. **5**, 150 (2024).

[14] B. Foxen *et al.*, Qubit compatible superconducting interconnects, Quantum Sci. Technol. **3**, 014005 (2017).

[15] N. P. de Leon, K. M. Itoh, D. Kim, K. K. Mehta, T. E. Northup, H. Paik, B. S. Palmer, N. Samarth, S. Sangtawesin, and D. W. Steuerman, Materials challenges and opportunities for quantum computing hardware, Science **372**, eabb2823 (2021).

[16] S. K. Choi, D.-H. Lee, S. G. Louie, and J. Clarke, Localization of metal-induced gap states at the metal-insulator interface: Origin of flux noise in squids and superconducting qubits, Phys. Rev. Lett. **103**, 197001 (2009).

[17] K. D. Crowley *et al.*, Disentangling losses in tantalum superconducting circuits, Phys. Rev. X **13**, 041005 (2023).

[18] M. P. Seah and W. A. Dench, Quantitative electron spectroscopy of surfaces: A standard data base for electron inelastic mean free paths in solids, Surf. Interface Anal. **1**, 2 (1979).

[19] J. E. Hamann-Borrero, S. Macke, B. Gray, M. Kareev, E. Schierle, S. Partzsch, M. Zwiebler, U. Treske, A. Koitzsch, B. Büchner, J. W. Freeland, J. Chakhalian, and J. Geck, Site-selective spectroscopy with depth resolution using resonant x-ray reflectometry, Sci. Rep. **7**, 13792 (2017).

[20] N. Cabrera and N. F. Mott, Theory of the oxidation of metals, Rep. Prog. Phys. **12**, 163 (1949).

[21] V. Somjit and B. Yildiz, Atomic and electronic structure of the Al_2O_3/Al interface during oxide propagation probed by ab initio grand canonical Monte Carlo, ACS Appl. Mater. Interfaces **14**, 42613 (2022).

[22] C.-E. Kim, K. G. Ray, and V. Lordi, A density-functional theory study of the $Al/AlO_x/Al$ tunnel junction, J. Appl. Phys. **128**, 155102 (2020).

[23] E. Tan, P. G. Mather, A. C. Perrella, J. C. Read, and R. A. Buhrman, Oxygen stoichiometry and instability in aluminum oxide tunnel barrier layers, Phys. Rev. B **71**, 161401(R) (2005).

[24] M. J. Cyster, J. S. Smith, N. Vogt, G. Opletal, S. P. Russo, and J. H. Cole, Simulating the fabrication of aluminium oxide tunnel junctions, npj Quantum Inf. **7**, 12 (2021).

[25] C. Zheng, K. Mathew, C. Chen, Y. Chen, H. Tang, A. Dozier, J. J. Kas, F. D. Vila, J. J. Rehr, L. F. J. Piper, K. A. Persson, and S. P. Ong, Automated generation and

ensemble-learned matching of x-ray absorption spectra, npj Comput. Mater. **4**, 12 (2018).
[26] K. Mathew, C. Zheng, D. Winston, C. Chen, A. Dozier, J. J. Rehr, S. P. Ong, and K. A. Persson, High-throughput computational x-ray absorption spectroscopy, Sci. Data **5**, 180151 (2018).
[27] M. K. Horton *et al.*, Accelerated data-driven materials science with the materials project, Nat. Mater. **24**, 1522 (2025).
[28] B. Watts, Calculation of the Kramers-Kronig transform of x-ray spectra by a piecewise Laurent polynomial method, Opt. Express **22**, 23628 (2014).
[29] B. L. Henke, E. M. Gullikson, and J. C. Davis, X-ray interactions: Photoabsorption, scattering, transmission, and reflection at E = 50–30, 000 ev, Z = 1–92, At. Data Nucl. Data Tables **54**, 181 (1993).
[30] A. Glavic and M. Björck, GenX 3: The latest generation of an established tool, J. Appl. Crystallogr. **55**, 1063 (2022).
[31] Ak Anbalagan, R. Cummings, C. Zhou, J. Mun, V. Stanic, J. Jordan-Sweet, J. Yao, K. Kisslinger, C. Weiland, D. Nykypanchuk, S. L. Hulbert, Q. Li, Y. Zhu, M. Liu, P. V. Sushko, A. L. Walter, and A. M. Barbour, Revealing the origin and nature of the buried metal-substrate interface layer in Ta/sapphire superconducting films, Adv. Sci. **12**, 2413058 (2025).
[32] A. B. Altman, C. D. Pemmaraju, S. Alayoglu, J. Arnold, C. H. Booth, A. Braun, C. E. Bunker, A. Herve, S. G. Minasian, D. Prendergast, D. K. Shuh, and T. Tyliszczak, Chemical and morphological inhomogeneity of aluminum metal and oxides from soft x-ray spectromicroscopy, Inorg. Chem. **56**, 5710 (2017).
[33] K. H. Stone, S. M. Valvidares, and J. B. Kortright, Kramers-Kronig constrained modeling of soft x-ray reflectivity spectra: Obtaining depth resolution of electronic and chemical structure, Phys. Rev. B **86**, 024102 (2012).
[34] A. B. Kuzmenko, Kramers–Kronig constrained variational analysis of optical spectra, Rev. Sci. Instrum. **76**, 083108 (2005).
[35] P. A. Dvortsova, A. M. M. Korovin, V. Ukleev, and S. M. Suturin, Blind fit modeling of soft x-ray resonant reflectivity maps in nanoscale epitaxial iron oxide multilayers, J. Appl. Phys. **135**, 055302 (2024).
[36] P. A. Dvortsova, A. M. Korovin, and S. M. Suturin, Intellectual fitting of hard x-ray resonant reflectance maps obtained for low-contrast oxide multilayers across L absorption edges of Eu and Gd, Mater. Today Commun. **41**, 110456 (2024).
[37] P. A. Dvortsova and S. M. Suturin, Applicability of energy-theta mapping in resonant soft x-ray reflectometry to probe depth dependence of oxidation state and crystallographic environment in iron oxide multilayers, Thin Solid Films **806**, 140517 (2024).
[38] See Supplemental Material at http://link.aps.org/supplemental/10.1103/lvjh-dxr8 for additional experimental details, data analysis, and supporting results.
[39] F. Reichel, L. P. H. Jeurgens, G. Richter, and E. J. Mittemeijer, Amorphous versus crystalline state for ultrathin Al_2O_3 overgrowths on Al substrates, J. Appl. Phys. **103**, 093515 (2008).
[40] A. Jain, S. P. Ong, G. Hautier, W. Chen, W. D. Richards, S. Dacek, S. Cholia, D. Gunter, D. Skinner, G. Ceder, and K. A. Persson, Commentary: The materials Project: A materials genome approach to accelerating materials innovation, APL Mater. **1**, 011002 (2013).
[41] D. Waroquiers, X. Gonze, G.-M. Rignanese, C. Welker-Nieuwoudt, F. Rosowski, M. Göbel, S. Schenk, P. Degelmann, R. André, R. Glaum, and G. Hautier, Statistical analysis of coordination environments in oxides, Chem. Mater. **29**, 8346 (2017).
[42] K.-I. Shimizu, Y. Kato, H. Yoshida, A. Satsuma, T. Hattori, and T. Yoshida, Al K-edge XANES study for the quantification of aluminium coordinations in alumina, Chem. Commun. **35**, 1681 (1999).
[43] K. Kimoto, Y. Matsui, T. Nabatame, T. Yasuda, T. Mizoguchi, I. Tanaka, and A. Toriumi, Coordination and interface analysis of atomic-layer-deposition Al_2O_3 on Si(001) using energy-loss near-edge structures, Appl. Phys. Lett. **83**, 4306 (2003).
[44] E. O. Filatova and A. S. Konashuk, Interpretation of the changing the band gap of Al_2O_3 depending on its crystalline form: Connection with different local symmetries, J. Phys. Chem. C **119**, 20755 (2015).
[45] J.-S. Oh, C. J. Kopas, H. Cansizoglu, J. Y. Mutus, K. Yadavalli, T.-H. Kim, M. Kramer, A. H. King, and L. Zhou, Correlating aluminum layer deposition rates, Josephson junction microstructure, and superconducting qubits' performance, Acta Mater. **284**, 120631 (2025).
[46] Dèle Bouchet and C. Colliex, Experimental study of elnes at grain boundaries in alumina: Intergranular radiation damage effects on Al-L_{23} and O-K edges, Ultramicroscopy **96**, 139 (2003).
[47] J. A. van Bokhoven, T. Nabi, H. Sambe, D. E. Ramaker, and D. C. Koningsberger, Interpretation of the Al K- and $L_{II/III}$-edges of aluminium oxides: Differences between tetrahedral and octahedral al explained by different local symmetries, J. Phys. Condens. Matter. **13**, 10247 (2001).
[48] C. Weigel, G. Calas, L. Cormier, L. Galoisy, and G. S. Henderson, High-resolution al $L_{2,3}$-edge x-ray absorption near edge structure spectra of al-containing crystals and glasses: Coordination number and bonding information from edge components, J. Phys. Condens. Matter. **20**, 135219 (2008).
[49] Z. Wang, C. Li, L. Liu, and T.-K. Sham, Probing defect emissions in bulk, micro- and nano-sized α-$A_{l2}O_3$ via x-ray excited optical luminescence, J. Chem. Phys. **138**, 084706 (2013).
[50] E. O. Filatova, A. S. Konashuk, S. S. Sakhonenkov, A. A. Sokolov, and V. V. Afanas'ev, Re-distribution of oxygen at the interface between γ-Al_2O_3 and TiN, Sci. Rep. **7**, 4541 (2017).
[51] J. G. Simmons, Low-voltage current-voltage relationship of tunnel junctions, J. Appl. Phys. **34**, 238 (1963).
[52] A. F. Harper, S. P. Emge, P. C. M. M. Magusin, C. P. Grey, and A. J. Morris, Modelling amorphous materials via a joint solid-state NMR and x-ray absorption spectroscopy and DFT approach: Application to alumina, Chem. Sci. **14**, 1155 (2023).
[53] D. Manuel, D. Cabaret, C. Brouder, P. Sainctavit, A. Bordage, and N. Trcera, Experimental evidence of thermal

fluctuations on the x-ray absorption near-edge structure at the aluminum *K* edge, Phys. Rev. B **85**, 224108 (2012).

[54] N. Amoyaw, A. Agegnehu, F. Sottile, M. Gatti, and M. L. Urquiza, Al *K*-edge xanes of octahedral aluminum compounds: Similarities and differences via the analysis of excitonic properties, Phys. Rev. B **111**, 165112 (2025).

[55] D. Cabaret, P. Sainctavit, P. Ildefonse, and A.-M. Flank, Full multiple scattering calculations on silicates and oxides at Al K-edge, J. Electron. Spectrosc. Relat. Phenom. **79**, 21 (1996).

[56] S. Oh, K. Cicak, J. S. Kline, M. A. Sillanpää, K. D. Osborn, J. D. Whittaker, R. W. Simmonds, and D. P. Pappas, Elimination of two level fluctuators in superconducting quantum bits by an epitaxial tunnel barrier, Phys. Rev. B **74**, 100502(R) (2006).

[57] L. G. Parratt, Surface studies of solids by total reflection of x-rays, Phys. Rev. **95**, 359 (1954).

[58] G. Kresse and J. Hafner, *Ab initio* molecular dynamics for liquid metals, Phys. Rev. B **47**, 558 (1993). publisher: APS

[59] G. Kresse and J. Hafner, *Ab initio* molecular-dynamics simulation of the liquid-metal–amorphous-semiconductor transition in germanium, Phys. Rev. B **49**, 14251 (1994).

[60] G. Kresse and J. Hafner, Norm-conserving and ultrasoft pseudopotentials for first-row and transition elements, J. Phys. Condens. Matter. **6**, 8245 (1994).

[61] G. Kresse and D. Joubert, From ultrasoft pseudopotentials to the projector augmented-wave method, Phys. Rev. B **59**, 1758 (1999).

[62] G. Kresse and J. Furthmüller, Efficiency of ab-initio total energy calculations for metals and semiconductors using a plane-wave basis set, Comput. Mater. Sci. **6**, 15 (1996).

[63] G. Kresse and J. Furthmüller, Efficient iterative schemes for *ab initio* total-energy calculations using a plane-wave basis set, Phys. Rev. B **54**, 11169 (1996).

[64] I. Batatia, S. Batzner, D. P. Kovács, A. Musaelian, G. N. C. Simm, R. Drautz, C. Ortner, B. Kozinsky, and G. Csányi, The design space of E(3)-equivariant atom-centered interatomic potentials, arXiv:2205.06643.

[65] I. Batatia, D. P. Kovacs, G. N. C. Simm, C. Ortner, and G. Csanyi, MACE: Higher order equivariant message passing neural networks for fast and accurate force fields, *Advances in Neural Information Processing Systems*, edited by A. H. Oh-A. Agarwal-D. Belgrave-K. Cho (Curran Associates, Inc., Red Hook, NY, 2022).

[66] Y. Ma, N. Wassdahl, P. Skytt, J. Guo, J. Nordgren, P. D. Johnson, J.-E. Rubensson, T. Boske, W. Eberhardt, and S. D. Kevan, Soft-x-ray resonant inelastic scattering at the C K edge of diamond, Phys. Rev. Lett. **69**, 2598 (1992).

[67] M. Taillefumier, D. Cabaret, A.-M. Flank, and F. Mauri, X-ray absorption near-edge structure calculations with the pseudopotentials: Application to the K edge in diamond and α-quartz, Phys. Rev. B **66**, 195107 (2002).